HighPressure Homogenization: An Industrially Scalable Method for Producing PHBH Powders for Selective Laser Sintering

ADVANCED MATERIALS TECHNOLOGIES
www.advmattechnol.de

High-Pressure Homogenization: An Industrially Scalable Method for Producing PHBH Powders for Selective Laser Sintering

Alberto Giubilini, Giovanna Colucci, Silvia Grasselli, Luca Iuliano, Massimo Messori, and Paolo Minetola*

Selective laser sintering (SLS) enables the production of high-quality, complex plastic components without requiring support structures. However, the widespread adoption of SLS is constrained by limited material availability, mainly synthetic polymers, and the inefficiency of laboratory-scale methods, such as solvent phase separation, for producing new polymer powders. This study explores high-pressure homogenization (HPH) as a purely mechanical and solvent-free method for micronizing poly(3-hydroxybutyrate-*co*-3-hydroxyhexanoate) (PHBH), a biodegradable co-polyester, into particles suitable for SLS. The influence of key HPH parameters, including pressure and number of passes, on particle morphology and size distribution is evaluated. Under optimal conditions, 18 passes at 1000 bar, a median particle size of 49 µm is achieved, with powders exhibiting sub-rounded morphology (median circularity of 0.944) and sufficient flowability, as indicated by a Hausner ratio of 1.34, making them suitable for SLS processing. The 3D printability is tested on both simple and complex geometries, which all result in 95% dense final components. Thermal characterization indicates that the PHBH powders retain suitable thermal stability, with degradation temperatures exceeding the SLS processing range. Mechanical testing of 3D printed parts reveals Young's modulus of 160 MPa and a maximum storage modulus of 2.7 GPa at −10 °C.

1. Introduction

Additive manufacturing (AM) of polymers is increasingly adopted for producing advanced plastic components across diverse industries, including automotive, electronics, biomedical, and aerospace.[1–4] Among the various AM techniques, material extrusion and vat photopolymerization are widely used due to their accessibility and user-friendliness, making them attractive to both hobbyists and professionals. However, material extrusion often results in coarse resolution,[5] and vat photopolymerization employs thermoset resins that are difficult to recycle.[6]

Selective Laser Sintering (SLS), a powder-based AM process, fabricates complex 3D structures by sintering polymer powders with a laser beam. Compared to extrusion-based approaches, SLS provides higher part isotropy and enables full saturation of the build volume through 3D nesting, enhancing productivity. Moreover, it eliminates the need for support structures.[7]

Despite these advantages, the broader adoption of SLS is constrained by the comparatively limited variety of commercially available polymer materials. Currently, most SLS applications rely on synthetic polymers such as polyamides (PA), thermoplastic elastomers (TPE), polystyrene (PS), polyetherketoneketone (PEKK), and polyetheretherketone (PEEK).[8] While this limitation may be less evident in certain regions or specific research environments, expanding the available feedstock for SLS remains a global challenge. Recent studies have explored novel polymers for SLS, such as poly(L-lactic acid) (PLLA),[9] polycaprolactone (PCL),[10] polyvinylidene fluoride

A. Giubilini, L. Iuliano, P. Minetola
Department of Management and Production Engineering (DIGEP)
Politecnico di Torino
Corso Duca degli Abruzzi 24, Torino 10129, Italy
E-mail: alberto.giubilini@polito.it

The ORCID identification number(s) for the author(s) of this article can be found under https://doi.org/10.1002/admt.202500049

DOI: 10.1002/admt.202500049

A. Giubilini, G. Colucci, L. Iuliano, M. Messori, P. Minetola
Integrated Additive Manufacturing Centre (IAM@PoliTO)
Politecnico di Torino
Corso Duca degli Abruzzi 24, Torino 10129, Italy

G. Colucci, M. Messori
Department of Applied Science and Technology (DISAT)
Politecnico di Torino
Corso Duca degli Abruzzi 24, Torino 10129, Italy

S. Grasselli
GEA Mechanical Equipment Italia S.p.A.
Via Angelo Maria da Erba Edoari 29/A, Parma 43123, Italy

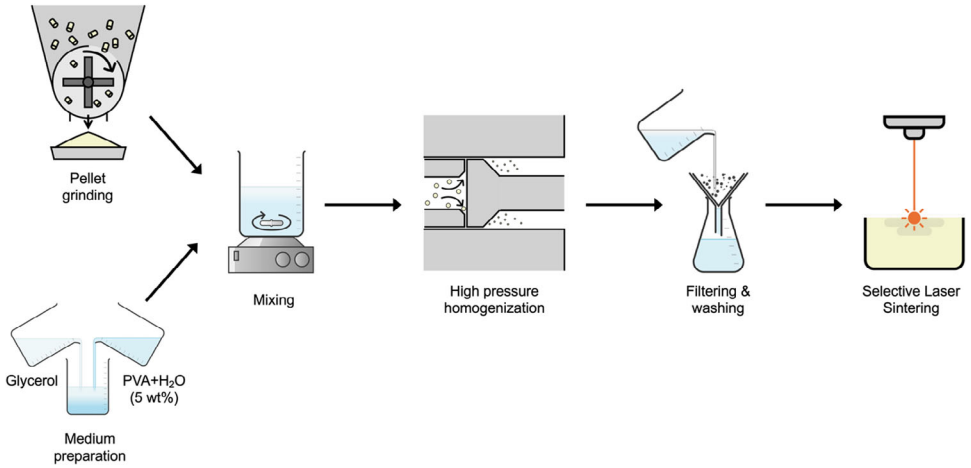

Figure 1. Schematic representation of the research workflow.

(PVDF),[11] and polymethyl methacrylate (PMMA),[12] yet most remain at experimental or pre-commercial stages.

In parallel, increasing concern over the environmental impact of nonrenewable materials is accelerating the search for biodegradable and bio-based alternatives, which could broaden the applicability of SLS while supporting sustainability goals.[13] Biopolymers have thus emerged as promising candidates for AM.[14,15] In particular, the polyhydroxyalkanoate (PHA) family has attracted attention due to its tunable mechanical properties, cytocompatibility, and biodegradability under diverse environmental conditions.[16,17] Within this family, poly(3-hydroxybutyrate-co-3-hydroxyhexanoate) (PHBH) is a bacterial-fermentation-derived aliphatic co-polyester that offers a compelling balance of strength and flexibility, positioning it as a potential alternative to conventional plastics like polypropylene.[18,19]

Previous work with PHA-based powders for SLS has mainly focused on biomedical applications, demonstrating biocompatibility and scaffold fabrication capabilities.[20–22] However, biopolymer powder production for SLS has primarily relied on solvent-based methods,[23–27] which present scalability and environmental drawbacks due to their reliance on volatile organic compounds.

This study explored an alternative, solvent-free method to produce PHBH powder using the high-pressure homogenization (HPH) method, a purely mechanical process potentially capable of producing fine, uniform particles tailored for SLS. While other mechanical micronization methods, including cryo-milling,[28] ball-milling, rotor-milling, and spray drying,[29,30] have been explored, HPH was explored in this study due to its scalability, potential to produce powders with narrow particle size distributions, minimal thermal degradation. The effectiveness of the HPH process, as well as the influence of homogenization pressure and number of passes, was assessed in terms of powder morphology, particle size distribution, and flowability. Following 3D printing, the fabricated components were characterized with respect to their thermal properties, tensile and dynamic-mechanical performance, and dimensional accuracy.

The novelty and the technological significance of this study lie in the application of a still under-explored technique for powder production, employed here, to the best of the authors' knowledge, for the first time using industrial-scale equipment rather than laboratory-scale setups. This study covers the entire workflow from powder fabrication to 3D printing and final part characterization. While PHBH was chosen for its attractive properties, the proposed method is not limited to this polymer and may be extended to other materials suitable for SLS.

2. Experimental Section

2.1. Materials and Equipment

Poly(3-hydroxybutyrate-*co*-3-hydroxyhexanoate) (PHBH) pellet was purchased by MAIP Group (MAIP S.r.l., Settimo Torinese, Italy) with a density of 1.22 g cm^{-3} and a composition ratio of 89 mol% of 3-hydroxybutyrate (3HB) and 11 mol% of 3-hydroxyhexanoate (3HH), as reported by the supplier's datasheet. Poly(vinyl alcohol) (PVA) 8–88 was supplied from Merck (Merck KGaA, Darmstadt, Germany), and glycerol EP 99% was supplied by ACEF (ACEF SpA, Fiorenzuola d'Arda, Italy). Silica oxide was supplied by Merck (Merck KGaA, Darmstadt, Germany). All materials were used as received, without further purification.

2.2. PHBH Powder Preparation

The production process of PHBH powder is illustrated in **Figure 1** and involves four main steps: initial grinding of the PHBH pellets, preparation of the medium suspension, high-pressure homogenization (HPH), and final washing, and drying.

Initially, the PHBH pellets were cryo-ground using liquid nitrogen and an A10 basic mill (IKA, Staufen, Germany), and then sieved through a 1 mm mesh size sieve. The ground biopolymer was dispersed at a concentration of 1 wt.% in a liquid medium composed of 50 wt.% glycerol and 50 wt.% of an aqueous

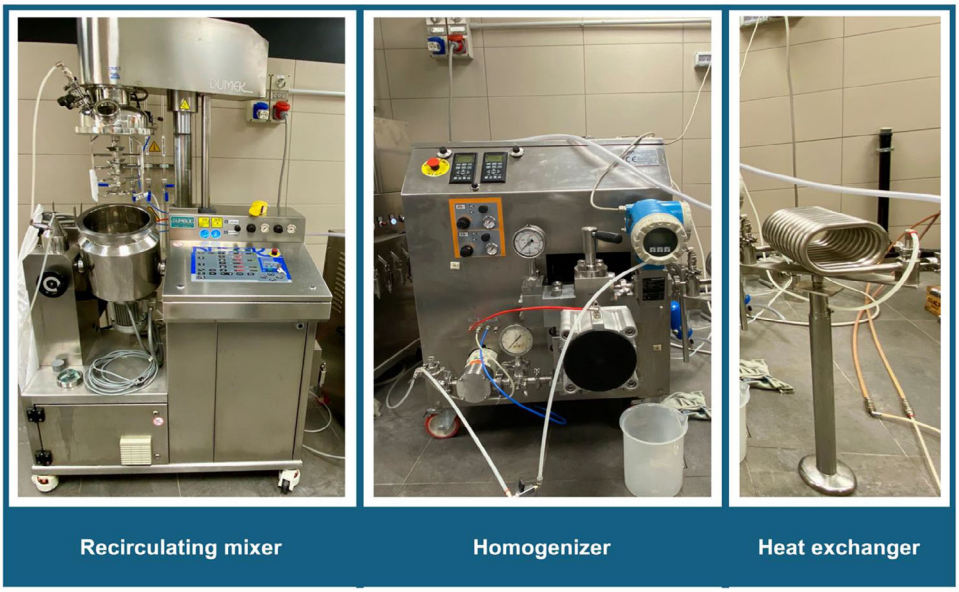

Figure 2. Photographs of the homogenization setup consisting of: a recirculating mixer, NS3006L homogenizer, and heat exchanger.

solution containing 5 wt.% of PVA. The composition of this dispersion was determined through preliminary tests to achieve a stable suspension with suitable viscosity for pumpability during the homogenization process while preventing gravitational separation (see Supporting Information). Specifically, PVA was used as a surfactant to enhance dispersion stability and prevent particle aggregation, while glycerol reduced the density difference between the solid and liquid phases, slowing down settling or skimming. The PHBH suspension was processed in the laboratories of GEA Mechanical Equipment. First, it was mixed with a high-shear mixer at 3000 rpm. Then, it was homogenized with a Panther NS3006L homogenizer (GEA Mechanical Equipment, Parma, Italy), which was equipped with a single homogenizing stage, a pumping system for abrasive and viscous products, and a heating exchanger. **Figure 2** shows the homogenization setup. The processing involved two steps: two passes at 300 bar, followed by multiple passes at two different homogenization pressures, namely 800 and 1000 bar. The sample nomenclature used in this manuscript was as follows: PHBH_NH refers to the not homogenized PHBH powder, while PHBH_X_Y denotes the homogenized powders, where X represents the number of passes and Y indicates the homogenization pressure in bar. After homogenization, the resultant powder was filtered, repeatedly washed with distilled water, and oven-dried at 50 °C overnight. The effectiveness of the washing process was evaluated by Fourier transform infrared spectroscopy (FT-IR) using ATR analysis. In particular, the spectrum of PHBH_18_1000 was compared with those of the neat PHBH pellet, PVA, and glycerol. No characteristic peaks of glycerol or PVA were detected in the PHBH_18_1000 sample, confirming their successful removal. Detailed spectra were reported in the Supporting Information. The dried powder was subsequently sieved with a 100 µm mesh sieve. Due to its tendency to pack, the micronized powder exhibited poor flowability, as demonstrated by compressibility and flowability test results in the Supporting Information). To enhance powder layer distribution during the SLS process, the powder was mixed with 0.25 wt.% silica oxide for 30 min, following a method previously reported in the literature to improve the flowability of laboratory-produced polymer powders.[31,32] A more in-depth discussion of the effect of silica oxide addition on flowability was reported in the Supporting Information.

2.3. PHBH Powder Characterization

The PHBH powder morphology was analyzed with a Phenom XL G2 Desktop scanning electron microscope (Thermo Fisher Scientific, Waltham, Massachusetts, USA) at an accelerating voltage of 20 kV. The powder was previously sputter-coated with gold for 3 min at 10^{-3} mbar and 10 mA current flow (Complete Sputter Coating System, West Chester, Pennsylvania, USA).

The particle size distribution was evaluated using a Mastersizer 3000 laser granulometer (Malvern Panalytical, Malvern, United Kingdom). This instrument employs laser diffraction to determine the particle size distribution of powders suspended in water. Signal processing was conducted using the Fraunhofer mathematical model. The span was calculated according to the following equation:

$$Span = \frac{D_{90} - D_{10}}{D_{50}} \quad (1)$$

where D_{10}, D_{50}, and D_{90} correspond to the particle sizes at which 10%, 50%, and 90% of the total volume of particles were smaller than those sizes, respectively.

The thermal stability of PHBH powder was analyzed using a Mettler-Toledo TGA 851e instrument (Mettler Toledo, Columbus, Ohio, USA). Samples underwent a heating ramp from 25 to 800 °C at a rate of 10 °C min^{-1} under an airflow of 50 mL min^{-1}. All TGA curves were normalized to the samples' unit weight.

The melting and crystallization behaviors of the samples were measured through DSC analyses before and after the HPH. The tests were performed with a DSC 214 Polyma device (Netzsch Group, Selb, Germany) under a nitrogen flow of 40 mL min^{-1} from −50 to 200 °C. The thermal transitions were recorded during the heating and cooling scans. A consistent heating/cooling rate of 10 °C min^{-1} was maintained throughout all cycles. The degree of crystallization (X_c) was calculated using Equation (2):

$$X_c = \frac{\Delta H_m - \Delta H_{cc}}{\Delta H_m^0} \times 100 \quad (2)$$

where ΔH_m, ΔH_{cc}, ΔH_m^0 represent the enthalpy of fusion, the enthalpy of cold crystallization, and the enthalpy of fully crystalline PHBH (115 J g^{-1}),[33] respectively.

The flowability of the PHBH powder was evaluated by determining the packing factor (φ), the compressibility index (C), the Hausner ratio (HR), and the angle of repose (AOR). C, HR, and φ parameters were measured following a simplified version of the ASTM D7481 standard, using a 25 mL graduated cylinder, according to Equations (3)–(5):

$$\varphi = \frac{\rho_{bulk}}{\rho} \quad (3)$$

$$C = \frac{\rho_{tap} - \rho_{bulk}}{\rho_{tap}} \times 100 \quad (4)$$

$$HR = \frac{\rho_{tap}}{\rho_{bulk}} \quad (5)$$

where ρ, ρ_{bulk}, ρ_{tap} represent the true, apparent, and tapped densities of the PHBH powder, respectively. The AOR was also used to assess the flowability of the processed powder. In this method, the powder passes through a funnel with a 5 mm orifice, and the AOR was measured as the angle between the slope of the powder pile and the horizontal plane, following Equation (6):

$$AOR = \tan^{-1}\left(\frac{2h}{D}\right) \quad (6)$$

where h is the height of the conical pile, and D is the average diameter of the powder pile measured from five different positions.

The true density (ρ) of the PHBH powder was determined using an Ultrapyc 5000 gas pycnometer (Anton Paar GmbH, Graz, Austria) with helium as the probe gas. A sample of ≈3.8 g of powder was placed in the "small" sample cell, and the density was measured at 20 °C using the "pulse" preparation mode and the "fine powder" flow mode. A minimum of 3 passes was conducted, with three measurements per pass, and a final precision criterion of 0.02% was set.

2.4. Selective Laser Sintering (SLS)

All samples were manufactured using a SnowWhite^2 SLS machine (Sharebot S.r.l., Nibionno, Italy) equipped with a CO_2 laser beam operating at a wavelength of 10.6 µm. The biopolymer powder was evenly distributed by a blade recoater under ambient air conditions. The processing temperature was controlled by monitoring the overall build chamber temperature, referred to as the environmental temperature, using a thermocouple. The environmental temperature was set to 90 °C, based on the sintering window identified through DSC characterization and in agreement with a previously published study.[34] Once the target environmental temperature was reached, a waiting time of 300 s was set to ensure uniform heating of the powder bed. The key processing parameters were enlisted in **Table 1**.

Table 1. Selective laser sintering process parameters.

Process parameters	
Laser power [W]	3.5
Scan speed [m s^{-1}]	2.4
Border scan speed [m s^{-1}]	3.3
Layer height [mm]	0.1
Environmental temperature [°C]	90
Number of warming layers	50–150

Three different geometries were produced using the same powder. Initially, simple bars were 3D printed for tensile and dynamic-mechanical analysis. Subsequently, more complex shapes, such as a boat and a geometry composed of overlapping polyhedron, were manufactured to evaluate the 3D printability of the obtained homogenized powder with more challenging designs.

2.5. 3D Printed Parts Characterization

Thermogravimetric analysis (TGA) was carried out on the 3D printed samples using a Mettler-Toledo TGA 851e Instrument (Columbus, OH, USA), from 25 to 800 °C with a heating rate of 10 °C min^{-1} and 50 mL min^{-1} of airflow.

Differential scanning calorimetry (DSC) analysis was performed on the 3D printed samples using a Netzsch 214 Polyma Equipment (Selb, Germany) from −50 to 180 °C with a heating/cooling rate of 10 °C min^{-1} with a nitrogen flow of 40 mL min^{-1}. Two heating and one cooling scan were done to determine the thermal transitions.

Dynamic-mechanical analysis (DMA) was carried out by using an MCR 702e Multidrive Device (Anton Paar, Graz, Austria), by applying a uniaxial sinusoidal stress with an amplitude of 1 N and a frequency of 1 Hz on rectangular samples with dimensions of length of 35 mm, a width of 10 mm, and a thickness of 1 mm.

Uniaxial tensile tests were performed using a Z3 tensile testing machine (AML Instruments, Lincoln, United Kingdom) at a crosshead speed of 1 mm min^{-1}. Five 3D printed specimens were tested, each with dimensions of 35 mm in length, 10 mm in width, and 1 mm in thickness.

A micro-CT scanner, model Phoenix v|tome|x S240 (GE Baker Hughes-Waygate Technologies, Wunstorf, Germany) was utilized to inspect the 3D printed specimens. The X-ray scanning parameters for the boat model were set to a voxel size of 49.2 µm, 210 kV voltage, 130 µA current, 100 ms exposure time, and 1500 images, whereas for the open cell lattice structure, they were 36.9 µm, 120 kV, 100 µA, 333 ms, and 1500 images. Reconstruction of the X-ray images into 3D models was performed

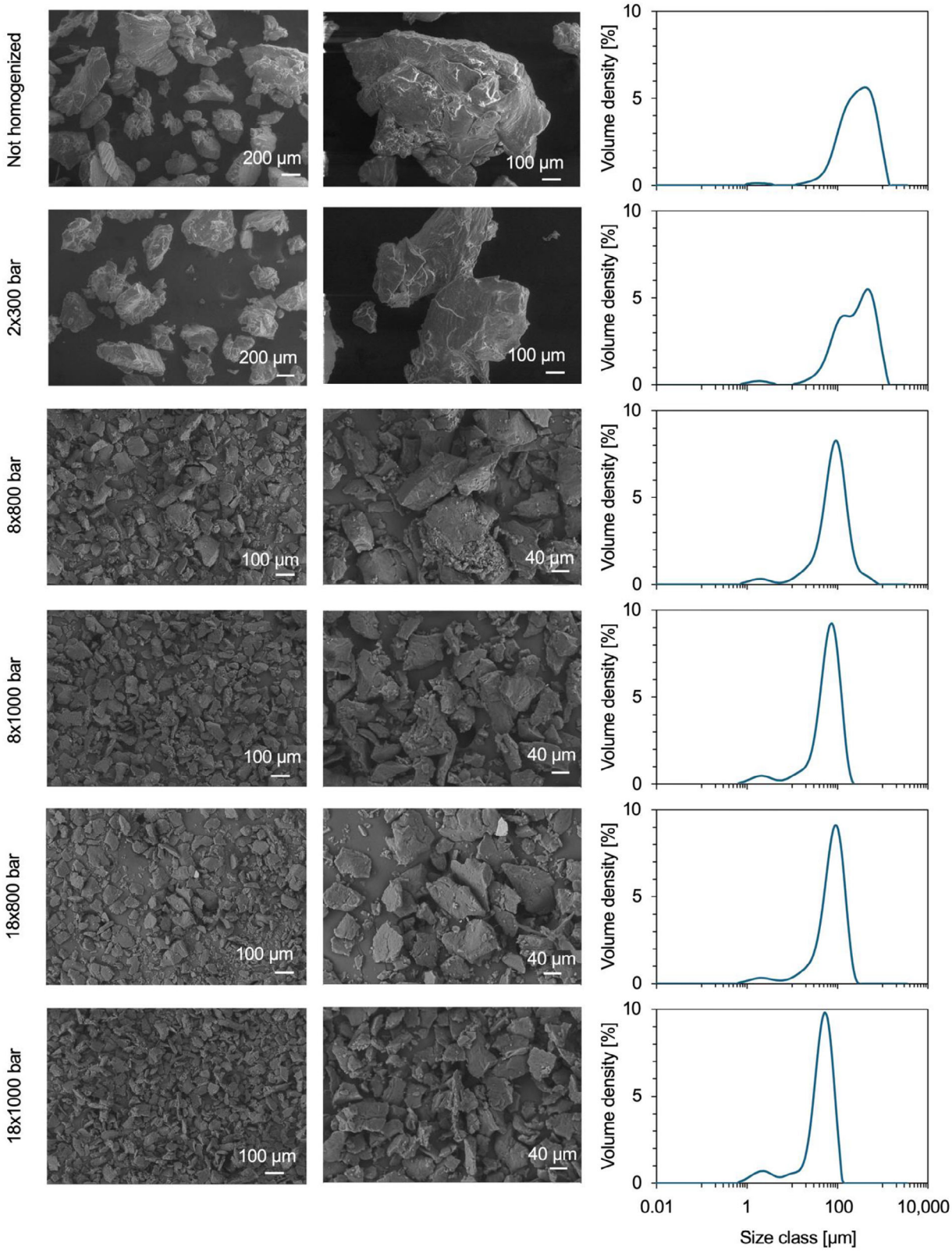

Figure 3. SEM micrographs and particle size granulometric curves of PHBH powders obtained at different homogenizing conditions.

using datos|reconstruction software, while VG Studio Max (version 3.4, Volume Graphics, Hexagon Metrology-Volume Graphics, Heidelberg, Germany) was employed for visualization and analysis. Prior to dimensional analysis, surface determination was conducted using the *Advanced (classic)* approach. This process began with contour identification from the histogram, employing an *Automatic* material definition at an isovalue threshold of 50%. Based on the results of the surface determination, the *nominal/actual comparison analysis* module within VG Studio software was applied to evaluate the accuracy of the 3D printed specimens.

The bulk density of the 3D printed samples was determined using the Archimedes method, in accordance with the ASTM B962–17 standard. Given that the tested biopolymer material has a density close to 1 g cm^{-3}, isopropyl alcohol was used as the immersion liquid instead of distilled water to improve measurement accuracy. Five different specimens were analyzed to ensure statistical significance. The porosity (P) of the samples was calculated using Equation (7):

$$P = \frac{\rho - \rho_{sls}}{\rho} \times 100 \tag{7}$$

where ρ_{sls} represents the measured density of the 3D printed sample and ρ is the true density of the PHBH powder, which was determined using the gas pycnometer.

The ρ_{sls} values were calculated using two different approaches: the total porosity, as defined by Equation (8), and the closed porosity, as defined by Equation (9):

$$\rho_{sls} = \frac{W_{air} \times \rho_{liq}}{W_{fin} - W_{liq}} \tag{8}$$

$$\rho_{sls} = \frac{W_{air} \times \rho_{liq}}{W_{air} - W_{liq}} \tag{9}$$

where W_{air}, $W_{liq,}$ and W_{fin} represent the mass of the sample in air, the mass while immersed in the liquid, and the mass after removal from the liquid, respectively. ρ_{liq}, the density of the isopropyl alcohol used for immersion, was 0.785 g cm^{-3}.

Table 2. Evaluation of temperature variations during the HPH process.

Number of passes	Homogenizer inlet temperature [°C]	Homogenizer outlet temperature [°C]	Heat exchanger outlet temperature [°C]
1	24	38.0	33.0
2	24	37.0	32.0
3	26	53.5	42.5
5	33	60.0	44.5
10	39	63.5	46.5
13	40	66.0	47.0
15	40	66.5	47.5
17	41	66.5	47.5
20	40	66.5	46.5

3. Results and Discussion

3.1. Morphology of PHBH Powder Obtained by HPH

A preliminary evaluation of the processability of PHBH via HPH was conducted to determine the optimal dispersibility and pumpability. Various solid-to-medium ratios and liquid-medium compositions were tested, with the formulation presented in this study yielding the most stable yet pumpable dispersion of PHBH, suitable for homogenizer processing. All homogenization processes began with two initial passes at a low pressure of 300 bar to break down the largest biopolymer particles and prevent clogging of the homogenizing valve. Subsequently, two different pressure drops were assessed, with measurements taken after 8 and 18 passes, respectively.

Another critical aspect to be considered when assessing the applicability of new powder material for SLS applications is the morphology and particle size distribution. Previous research has well-established that SLS polymer particles should be near-spherical to achieve optimal flowing spreadability, with particle sizes ranging between 10 and 100 µm.[35] To characterize the powder's size and shape, SEM analysis was performed. **Figure 3** clearly illustrates the impact of both the number of homogenization passes and pressure on PHBH powders, showing that average particle size decreases with an increase in either passes or pressure. This reduction in particle size results from several contributions, namely compression, cavitation induced by pressure drop, shear forces, and impact over the homogenizing ring.[36,37]

The SEM images revealed that all powders exhibited an irregular morphology. This deformation could be attributed to plastic deformation of PHBH particles during processing, as the homogenization process increases operating temperatures that can reach up to almost 70 °C, as reported in **Table 2**. These high temperatures, combined with high pressures, may contribute to the particle's plastic deformation, resulting in nonspherical shapes.

To gain further insight into the powder morphology and confirm the size distribution, a granulometric analysis was also conducted. The resulting powder size distribution curves are represented in Figure 3, with corresponding data summarized in **Table 3**. The median distribution (D50) ranged from 313 µm for not homogenized PHBH to 75 and 49 µm after 18 passes

Table 3. Powder size distribution results at different homogenizing conditions.

Sample code	D_{10} [µm]	D_{50} [µm]	D_{90} [µm]	D_{100} [µm]	Span
PHBH_NH	105	313	727	1430	2.0
PHBH_1_800	61	193	564	1630	2.6
PHBH_3_800	47	144	430	1620	2.7
PHBH_8_800	28	90	198	855	1.9
PHBH_13_800	26	84	159	308	1.6
PHBH_18_800	23	75	143	240	1.6
PHBH_1_1000	56	166	416	1430	2.2
PHBH_3_1000	34	101	239	971	2.0
PHBH_8_1000	20	68	128	240	1.6
PHBH_13_1000	15	57	107	209	1.6
PHBH_18_1000	11	49	88	144	1.6

Table 4. True density (ρ), apparent density (ρ_{bulk}), tapped density (ρ_{tap}), and flowability properties of different powders: experimental PHBH_18_1000, commercial Aurora PA11 Wematter, commercial DuraForm PA12.

	PHBH_NH	PHBH_18_1000	PA11	PA12
ρ – True density [g cm^{-3}]	1.226 ± 0.003	1.226 ± 0.003	1.063 ± 0.002	1.050 ± 0.002
ρ_{bulk} – Apparent density [g cm^{-3}]	0.45 ± 0.01	0.42 ± 0.01	0.50 ± 0.01	0.44 ± 0.01
ρ_{tap} – Tapped density [g cm^{-3}]	0.66 ± 0.01	0.57 ± 0.01	0.58 ± 0.01	0.53 ± 0.01
HR – Hausner ratio factor	1.49 ± 0.01	1.34 ± 0.01	1.17 ± 0.01	1.20 ± 0.01
φ – Packing factor	0.36 ± 0.01	0.34 ± 0.01	0.46 ± 0.01	0.42 ± 0.01
C – Compressibility index [%]	32.6 ± 0.1	25.3 ± 0.1	14.3 ± 0.1	16.7 ± 0.1
Angle of repose [°]	36.3 ± 1.1	31.4 ± 1.6	29.5 ± 0.8	30.1 ± 0.7

at 800 bar and 1000 bar, respectively. These size distributions align with SEM observations and existing literature, supporting the suitability of these powders for SLS processing.[38]

Notably, most samples exhibited a single-peaked distribution, which became more uniform as homogenizing pressure and passes increased. This is evidenced by the narrowing of the distribution peak (Figure 3) and decreasing span values (Table 3), with low span values being an indirect indication of good powder spreading performance.[39] The narrowing effect is already notable after the initial pretreatment of 2 passes at 300 bar, where a shoulder emerges at lower particle sizes compared to not homogenized PHBH.

In summary, combining the analysis of powder morphology and particle size, the PHBH_18_1000, with the smallest particle size and improved uniformity, appeared the most suitable for SLS processing requirements. The granulometric analysis of PHBH_18_1000 powder revealed that the particles obtained by HPH are generally sub-rounded to rounded in shape, with a median circularity of 0.944. Accordingly, all subsequent characterizations and 3D printing trials were conducted using particles produced under these homogenizing conditions.

3.2. Flowability of PHBH Powder Obtained by HPH

The packing and flowability behaviors are two critical factors to consider when developing new powder fabrication processes or novel materials. Poor powder flowability can prevent the spreading of a dense, defect-free powder layer, which in turn compromises the efficiency of the sintering process. To address this potential issue, the packing and flowability properties of PHBH_18_1000 powders were evaluated by first determining the true density, followed by Hall flow and tap density tests. Key results are summarized in **Table 4**.

An important finding is the average true density of PHBH_18_1000 powder, measured by gas pycnometry at 1.226 ± 0.003 g cm^{-3}. This value matches with the supplier's datasheet for the neat PHBH pellets, suggesting that the homogenization process successfully produces fully dense PHBH powders.

Additionally, a comparative analysis of the main flowability properties was conducted for the PHBH particles before (PHBH_NH) and after HPH treatment (PHBH_18_1000). Prior to homogenization, the PHBH powder exhibited poor flowability and, more critically, particle dimensions that were unsuitable for SLS applications. Following the HPH treatment, the particle size distribution was brought within a more appropriate range, leading to an improvement in flowability. For example, the Hausner ratio decreased from 1.49 to 1.34, and the angle of repose also diminished from 36.3° to 31.4°.

According to Carr's classification of flow behavior, based on the compressibility index and Hausner ratio, the PHBH_18_1000 powder is categorized as having "passable flowability."[40] To contextualize these experimental results, a comparison was made with two commercial SLS powders (PA11 and PA12), which exhibited the lowest Hausner ratios and angles of repose among the samples analyzed. These experimental results are consistent with previously published data, where commercial glass bead-reinforced PA12 powders[41] and neat PA12 powders[42] showed Hausner ratios ≈11% and 14% lower, respectively, than that of PHBH_18_1000. Although these characterizations provide indirect estimations of flowability and spreadability, it is reasonable to infer a slightly reduced flowability for PHBH powders compared to commercially available SLS powders. This inference is further supported by the powder's morphological analysis. It is well-known that particles with near-spherical shapes and regular sizes are more uniformly spread on the building platform by the recoating system.[43] In contrast, the irregular shapes of the PHBH_18_1000 powders correlate with reduced flowability.

Nevertheless, the angle of repose for PHBH_18_1000, measured at 31.4°, classifies it as "flowing," based on the proposed classification system,[44] and is consistent with the previously discussed flowability indicators. It is important to highlight, however, that previous studies demonstrated the successful printability of polymer-based composites with irregular morphologies in SLS processes.[41,45,46] Therefore, despite the suboptimal particle morphology and flow characteristics, the overall results from this preliminary characterization indicate that the PHBH powder produced via HPH exhibits flowability properties adequate for SLS applications.

3.3. Thermal Properties of PHBH Powder Obtained by HPH

TGA and DSC were conducted to investigate the thermal behavior of PHBH powders obtained by HPH, focusing on the thermal stability and degree of crystallinity. These analyses also provided insights into the sintering window, offering guidance for optimizing 3D printing conditions.

Figure 4 reports the TG curve and its derivative DTG for the homogenized PHBH powder, performed in air.

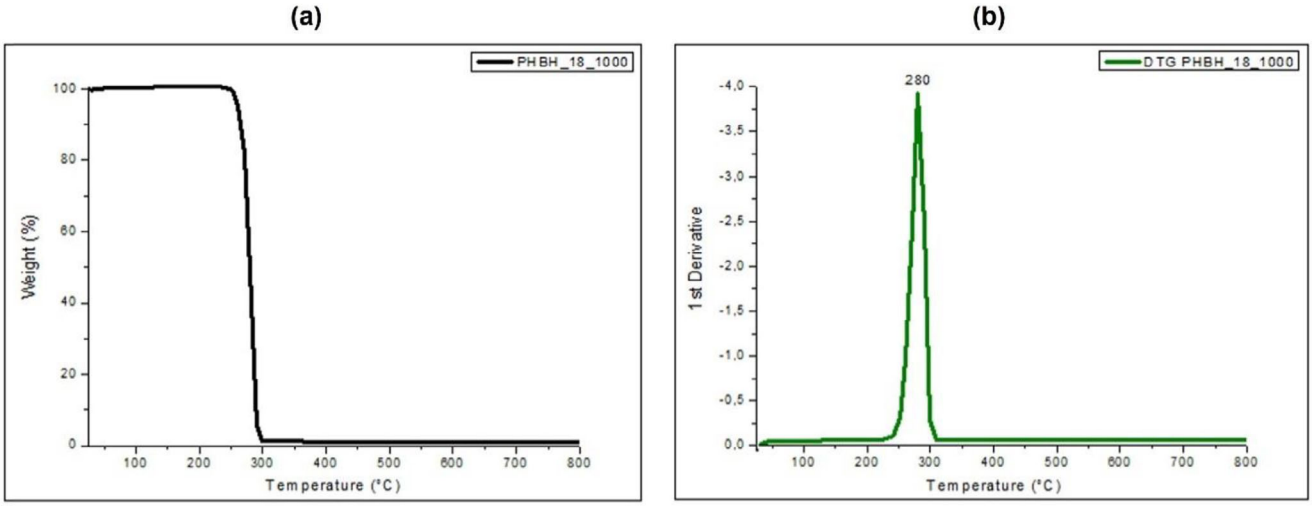

Figure 4. Thermal stability of PHBH powder obtained by HPH evaluated using TGA in air: thermogram a) and b) 1st derivative curve.

The TG curve indicates that the PHBH powder produced through HPH begins to degrade at 260 °C (Figure 4a). Degradation occurs in a single step, reaching its maximum rate at 280 °C, as shown by the DTG curve (Figure 4b). These results confirmed that the build chamber temperature (90 °C), at which the powder is maintained during the 3D printing process, is significantly lower than the thermal degradation temperature of the PHBH powder.

The DSC thermogram, reported in **Figure 5**, provides further insights into the thermal behavior of the PHBH powder obtained by HPH.

DSC analysis revealed a glass transition temperature at 0 °C, and a bimodal melting peak at 110 and 138 °C, which is characteristic of semicrystalline polyhydroxyalkanoates.[47] In the case of PHBH, the copolymer composition may influence the crystalline structure, particularly the formation and melting behavior of secondary lamellae, thereby accentuating the bimodal feature. During the second heating scan, an exothermic peak was observed at 52 °C, corresponding to the cold crystallization temperature. In addition, the melting and cold crystallization enthalpies were determined, and they were used to calculate the degree of crystallinity of the PHBH powder via Equation (2). The crystallinity was estimated to be ≈20%. DSC measurements were also employed to define the sintering window, a critical parameter for successful SLS processing. This window is typically defined as the temperature range between the onset of crystallization and the onset of melting. Based on the DSC data for PHBH powder, the sintering window was determined to lie between 63 and 94 °C. A summary of the TGA and DSC results is provided in **Table 5**.

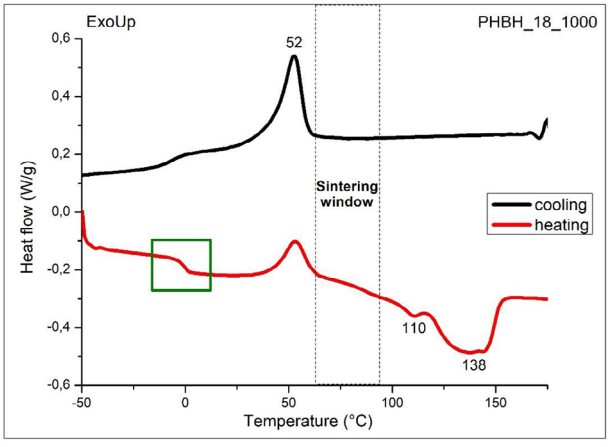

Figure 5. DSC curves of PHBH powder obtained by HPH evaluated in nitrogen.

3.4. Characterization of PHBH 3D Printed Components Obtained by SLS

To assess the suitability of the obtained PHBH powder as feedstock for SLS applications, initial tests involved producing 10-layer DMA samples, and their subsequent characterization. A first inspection revealed that the specimens exhibited solid structure, well-defined edges, and acceptable dimensional accuracy, with deviations constrained within 0.6% of the nominal dimensions. No layer delamination was observed; however, slight yellowing of the material and minor imperfections in surface flatness indicated that further optimization of the 3D printing parameters may be advantageous, although this lies beyond the scope of the current study.

3.5. Thermal Properties

The thermal properties of the 3D printed parts were evaluated by means of TGA and DSC, as similarly performed for the produced powder, and the results are illustrated in **Figure 6**.

The thermogram of the PHBH 3D printed specimen, reported in Figure 6a, clearly shows that the polymer degradation occurs in a single step, with a maximum degradation temperature of

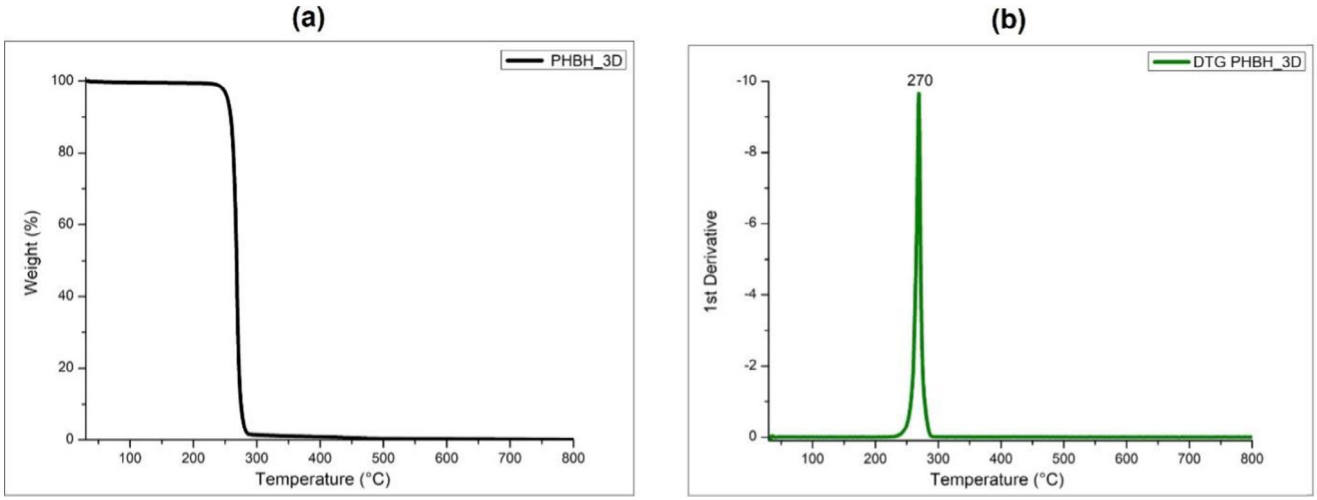

Figure 6. TG a) and DTG b) curves of 3D printed complex geometry obtained by SLS.

270 °C, as visible from the DTG curve of Figure 6b. This is consistent with the value of the PHBH powder, assessed at 280 °C, and aligns with previously published research on PHBH processed using different manufacturing technologies.[48–50] This result highlighted that the SLS process did not significantly affect the thermal stability of the biopolymer matrix. The glass transition temperature of the biopolymer, as determined by DSC (**Figure 7**), remained essentially unchanged following the SLS processing.

Additionally, the two melting peaks observed in the 3D printed part remained nearly identical to those of the original PHBH powder, located at ≈110 and 130 °C. However, a marked decrease in the degree of crystallinity was observed, dropping from 20% for the PHBH powder to 4% in the 3D printed part, as reported in Table 5. This substantial reduction may be attributed to the rapid cooling inherent to the SLS process, which limits the time available for polymer chains to realign into ordered crystalline domains. Therefore, a larger fraction of the material remains in the amorphous state, lowering the overall crystallinity. Despite this notable drop in crystallinity, the melting behavior of the material remains unaffected, suggesting that the SLS process only marginally alters the thermal transitions of the biopolymer.

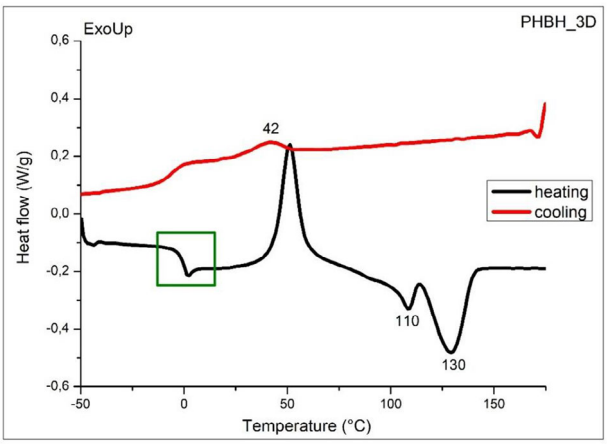

Figure 7. DSC curves of 3D-printed complex geometry obtained by SLS.

Table 6. Tensile properties of 3D printed PHBH specimens obtained via SLS.

Sample code	Young's modulus [MPa]	Ultimate tensile strength [MPa]	Strain at break [%]
PHBH_3D	161 ± 28	8.3 ± 1.2	11.6 ± 1.8

3.6. Mechanical Properties

The tensile characterization of SLS 3D printed specimens yielded a Young's modulus (E) of 161 MPa, an ultimate tensile strength (UTS) of 8.3 MPa, and a strain at break of 11.6%. The results, along with their standard deviations, are summarized in **Table 6**.

These values indicate moderate stiffness for PHBH processed via SLS. When compared to the manufacturer's datasheet

Table 5. Thermal properties of PHBH powder obtained by HPH and 3D printed part obtained via SLS.

Sample code	T_{onset} [a)] [°C]	$T_{max\ deg}$ [a)] [°C]	T_g [b)] [°C]	T_{m1} [b)] [°C]	T_{m2} [b)] [°C]	T_c [b)] [°C]	ΔH_m [b)] [J g^{-1}]	ΔH_{cc} [b)] [J g^{-1}]	X_c [%]
PHBH_18_1000	250	280	0	110	138	52	32.1	9.0	20
PHBH_3D	240	270	−1	110	130	42	32.7	27.7	4

[a)] Determined by TGA performed in the air; [b)] Determined by DSC performed in nitrogen.

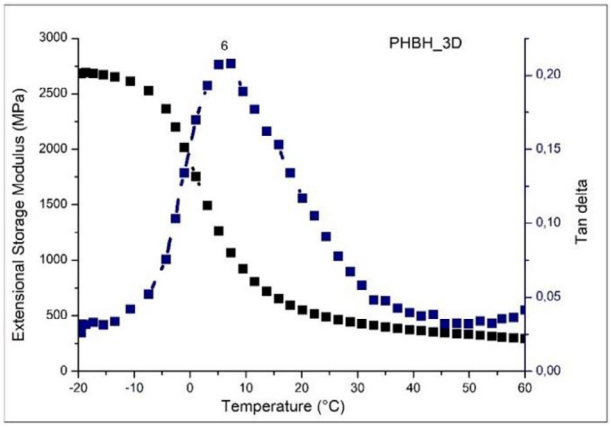

Figure 8. DMA curves of a 3D printed specimen of PHBH obtained by SLS.

values for bulk PHBH, typically obtained through injection or compression molding, Young's modulus is more than 5 times lower, and the UTS is approximately half. While direct comparisons with previously published mechanical characterizations of PHBH processed by SLS remain limited, the results observed here fall within a reasonable range for biopolymer specimens produced by SLS. The reduced mechanical performance can largely be attributed to the inherent characteristics of the AM process, including incomplete particle fusion, residual porosity, and suboptimal inter-layer bonding, all of which contribute to lower overall strength and stiffness. Although the optimization of mechanical properties and processing parameters was not the primary objective of this preliminary study, the findings clearly indicate that further work is needed to enhance the mechanical performance of components fabricated via SLS using biopolymer powders produced through HPH.

The viscoelastic properties of the 3D printed parts were evaluated using DMA analysis to assess their thermomechanical response. **Figure 8** illustrates the behavior of the extensional storage modulus and the tan delta values as a function of increasing temperature. The glass transition temperature of the 3D printed PHBH specimen, determined from the peak of the tan delta curve, is located at 6 °C. This value is higher with respect to that estimated by the DSC test, which was calculated at −1 °C. This discrepancy can be attributed to the inherent differences between the two techniques, as already reported in the literature.[51]

Figure 8 also reports the trend of the extensional storage modulus of the PHBH 3D printed specimen, which is ≈2.7 GPa evaluated in the rigid plateau region. This result underscores the suitability of combining this biopolymer powder with the SLS process, indicating its potential for semi-structural components, including the biomedical field.[52,53]

3.7. Microstructure

To better understand the effectiveness of the SLS process using the novel PHBH powder, the morphology of the PHBH 3D printed parts was examined through SEM analysis, focusing on the fracture surface of a 3D printed sample. **Figure 9** reports SEM images at different magnifications, 300× (a), 500× (b), and 1000× (c), showcasing the microstructure of a 3D printed component.

The lower magnification SEM image at 300× (Figure 9a) provides an overview of the cross-sectional morphology of the 3D printed samples, enabling the observation of larger features such as overall shape, pore distribution, and general homogeneity. This broader view helps identify macrostructural details that are not visible at higher magnification. As the magnification increases from 500 to 1000× (Figure 9b,c), the PHBH powder particles appear well-sintered, indicating that the 3D printing process was overall effective, starting from the PHBH powder produced via HPH. The specimen surface exhibited a smooth, fine-textured appearance. However, some areas exhibit incomplete sintering, likely due to the irregular shape of the powder particles, which may have hindered optimal particle coalescence during the SLS process, as well as the presence of amorphous regions in the processed PHBH powder. This observation aligns well with the previously reported degree of crystallinity of ≈20%. As noted in prior studies, amorphous regions may negatively influence the coalescence of PHBH powder particles. These regions, exhibiting higher chain mobility than crystalline areas, can cause

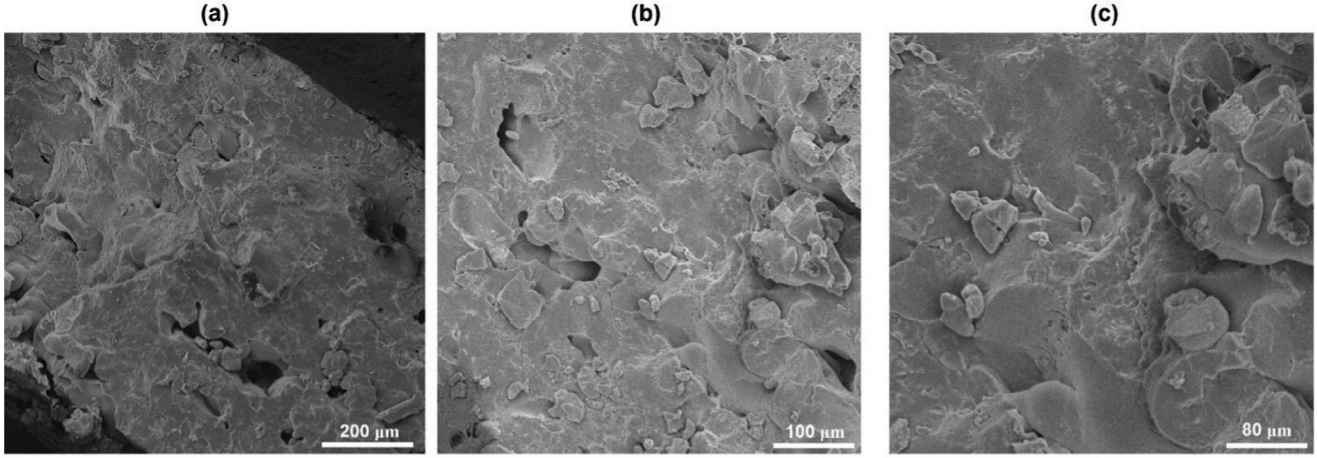

Figure 9. SEM micrographs of 3D printed components obtained by SLS at different magnifications: a) 300×, b) 500×, and c) 1000×.

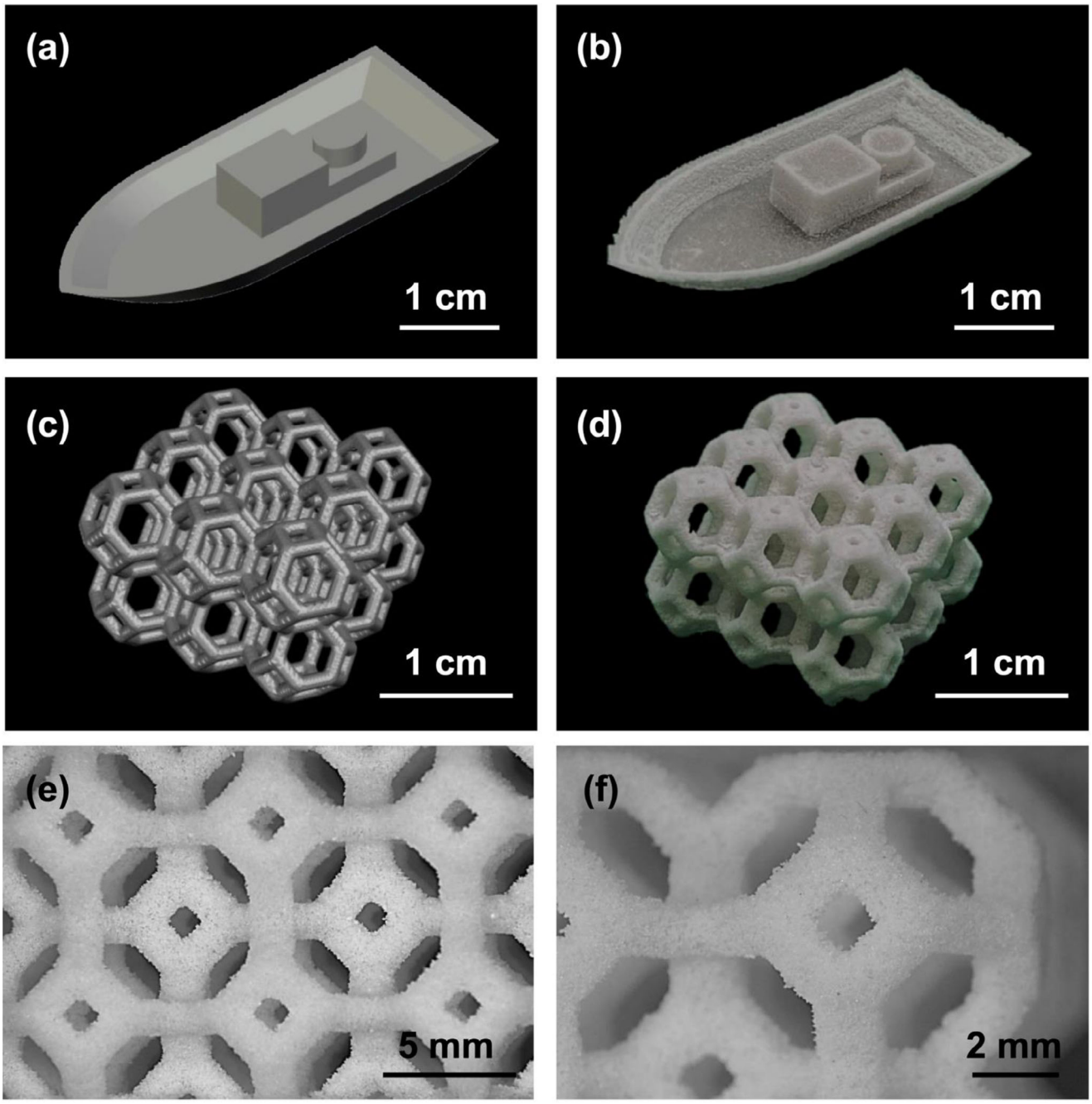

Figure 10. Representative view of 3D printed geometries obtained by SLS: a) STL representation of the miniature boat model; b) 3D printed miniature boat model; c) STL representation of the open-cell lattice structure; d) 3D printed open-cell lattice structure; e) optical microscope image of a lateral view of the open-cell lattice structure; f) optical microscope image of a detail of the open-cell lattice structure.

asynchronous melting behavior due to differences in melting temperatures. This mismatch in molten phase formation may hinder effective particle coalescence,[54] potentially leading to rougher surface morphology and increased porosity in the final part.[55] To confirm this, the density and porosity of the SLS printed parts were experimentally evaluated using the buoyancy method based on Archimedes' principle. The true density of the PHBH powder was determined via gas pycnometry to be 1.226 ± 0.003 g cm^{-3}. The density of the printed parts, based on closed porosity, was measured at 1.1530 ± 0.0015 g cm^{-3}, while the density considering total porosity was slightly higher at 1.1625 ± 0.0015 g cm^{-3}. From these values, the total porosity of the printed parts was calculated to be ≈5.2%, indicating satisfactory overall densification of the SLS parts.

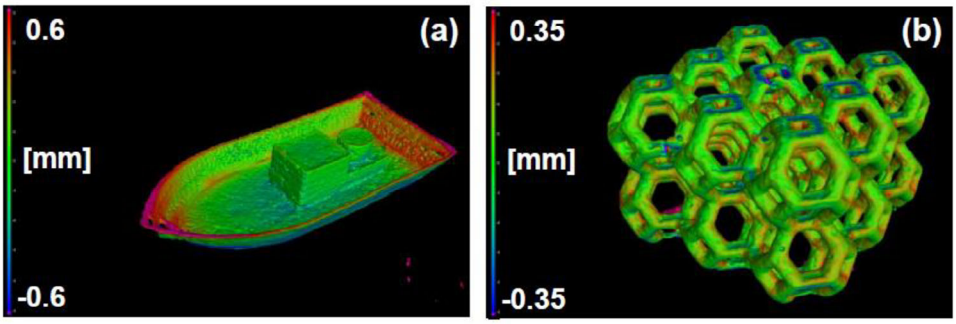

Figure 11. Colored deviation maps of actual geometry versus nominal geometry for two different 3D printed parts by SLS: a) boat model; b) open-cell lattice structure.

3.8. Selective Laser Sintering of Complex-Shaped PHBH Components

To further evaluate the 3D printability of this new powder using SLS, two more complex structures were fabricated: a miniature boat model and an open-cell lattice structure, consisting of two overlapping layers of 9 polyhedra with 16 faces each. **Figure 10** presents a visual comparison between the original designed model (Figure 10a,c) and the final 3D printing objects (Figure 10b,d). Specifically, the open-cell lattice structure consists of ≈150 layers in height, and it features intricate design elements such as 0.65 mm diamond-shaped holes, thin sloped walls angled up to 50°, and interconnected cell geometries with alternating solid and open spaces, as highlighted in the zoomed-in details (Figure 10e,f). Notably, the complexity and the final aspects of these 3D printed objects not only match but, in several aspects, surpass previously published results achieved with PHBH powder produced via solvent phase separation.[34] Therefore, these findings demonstrated that, despite the less spherical and regular morphology of the powder obtained via HPH, the 3D printability of the biopolymer powder is reliably maintained across a range of geometries, from simple to highly complex structures.

The 3D printing accuracy of the specimens was assessed using X-CT scans of the boat model and the open-cell lattice structure. These scans were aligned to the original CAD models via the *best-fit* registration function in VG Studio software, ensuring a precise overlay for comparison. Following alignment, deviations between the actual 3D printed geometries and their nominal designs were calculated. The results, presented in **Figure 11** as colored deviation maps, provide a visual and quantitative understanding of the dimensional accuracy.

When comparing the two geometries, the open-cell lattice structure demonstrated higher accuracy than the boat model. Specifically, the deviation range within which 90% of the surface area falls was calculated as 0.21 mm for the open-cell lattice structure, compared to 0.43 mm for the boat model. The greater deviations observed in the model can be attributed to the difficulty of realizing inclined thin walls. These features are particularly challenging for the 3D printing process, as they are more prone to material instability and potential distortions during printing.[56] These early findings are promising for the fabrication of geometries with high accuracy, suggesting that further research is worth optimizing the production of highly complex and accurate designs for SLS applications.

4. Conclusion

This study demonstrated the feasibility of HPH as a scalable, solvent-free, and more sustainable method for producing PHBH powders tailored for SLS applications. Compared to conventional solvent-based approaches such as phase separation, HPH offers a compelling alternative with greater industrial relevance. The process effectively reduced PHBH particles to the micron scale, achieving a median particle size of 49 µm under optimal conditions of 18 passes at 1000 bar. Despite the resulting powders exhibiting irregular morphology, flowability assessments, both direct and indirect, confirmed their suitability for SLS processing.

Thermal characterization revealed that the PHBH powders possess excellent thermal stability, with degradation temperatures significantly exceeding the SLS processing range. After the SLS process, the thermal stability and transition temperatures of the component remained almost unaffected. However, a reduction in crystallinity was observed, with the raw powder exhibiting 20% crystallinity, while the 3D printed components showed ≈4%. This decrease may have marginally hindered particle coalescence during sintering. Nevertheless, the HPH-produced powders exhibited satisfactory performance in SLS, enabling the fabrication of geometrically complex and dimensionally accurate components. SEM analysis and porosity calculations indicated a satisfactory degree of particle sintering, with a porosity value of 5.2%. These findings align with the dynamic mechanical properties, which showed a maximum storage modulus of ≈2.7 GPa in the plateau region, extending down to −10 °C, and Young's modulus at room temperature of 161 MPa.

While this research demonstrated significant progress in bridging laboratory-scale powder production with industrial demands, some limitations remain. Improving powder circularity could enhance packing density and mechanical performance in the final 3D-printed parts. Additionally, increasing the concentration of biopolymer suspended in the medium could improve HPH process efficiency and scalability. Future work should focus on optimizing SLS process parameters to improve the final part properties. Further investigation into the recyclability of the powders and continued refinement of their morphology and flowability would be beneficial for improving efficiency.

Although this study applied the HPH method to a specific biopolymer, it holds the potential to be extended to a wide range of biopolymers. This versatility could dramatically expand

material options available for SLS, thus fostering a more sustainable future in AM and supporting its ever-growing range of applications across various fields.

Supporting Information

Supporting Information is available from the Wiley Online Library or from the author.

Acknowledgements

This study was carried out within the Ministerial Decree no. 1062/2021 and received funding from the FSE REACT-EU – PON Ricerca e Innovazione 2014–2020. This manuscript reflects only the authors' views and opinions, neither the European Union nor the European Commission can be considered responsible for them. The authors are grateful to the R&D department of GEA Mechanical Equipment – Homogenizer (Parma, Italy), and particularly to Dr. Giovanni Gasparelli, Dr. Vincenzo Di Raimondo, and Dr. Alessio Ciuffreda for carrying out the homogenization process.

Conflict of Interest

The authors declare no conflict of interest.

Data Availability Statement

The data that support the findings of this study are available from the corresponding author upon reasonable request.

Keywords

additive manufacturing, biopolymer, high-pressure homogenization, PHBH, selective laser sintering

Received: January 7, 2025
Revised: April 23, 2025
Published online:

[1] S. Salifu, D. Desai, O. Ogunbiyi, K. Mwale, *Int. J. Adv. Manuf. Technol.* **2022**, *119*, 6877.
[2] Y. Yan, M. Han, Y. Jiang, E. L. L. Ng, Y. Zhang, C. Owh, Q. Song, P. Li, X. J. Loh, B. Q. Y. Chan, S. Y. Chan, *ACS Appl. Mater. Interfaces* **2024**, *16*, 5337.
[3] A. Das, C. A. Chatham, J. J. Fallon, C. E. Zawaski, E. L. Gilmer, C. B. Williams, M. J. Bortner, *Addit. Manuf.* **2020**, *34*, 101218.
[4] A. Giubilini, F. Bondioli, M. Messori, G. Nyström, G. Siqueira, *Bioengineering* **2021**, *8*, 29.
[5] G. D. Goh, Y. L. Yap, H. K. J. Tan, S. L. Sing, G. L. Goh, W. Y. Yeong, *Crit. Rev. Solid State Mater. Sci.* **2020**, *45*, 113.
[6] A. Davoudinejad, in *Handbooks in Advanced Manufacturing, Additive Manufacturing* (Eds.: J. Pou, A. Riveiro, J. Paulo Davim), Elsevier **2021**, pp. 159–181, https://doi.org/10.1016/B978-0-12-818411-0.00007-0.
[7] W. Han, L. Kong, M. Xu, *Int. J. Extreme Manuf.* **2022**, *4*, 042002.
[8] P. C. Gomes, O. G. Piñeiro, A. C. Alves, O. S. Carneiro, *Materials* **2022**, *15*, 5486.
[9] X. Gao, W. Deng, J. Tan, X. Shuai, J. Zan, T. Ye, K. Luo, F. Qi, Y. Wei, C. Shuai, *Mater. Today Chem.* **2025**, *43*, 102455.
[10] C.-H. Chen, V. B.-H. Shyu, J.-P. Chen, M.-Y. Lee, *Biofabrication* **2014**, *6*, 015004.
[11] C. Shuai, G. Liu, Y. Yang, F. Qi, S. Peng, W. Yang, C. He, G. Wang, G. Qian, *Nano Energy* **2020**, *74*, 104825.
[12] R. Velu, S. Singamneni, *J Mater. Res.* **2014**, *29*, 1883.
[13] S. RameshKumar, P. Shaiju, K. E. O'Connor, P. RB, *Curr. Opin. Green Sustain. Chem.* **2020**, *21*, 75.
[14] M. Mehrpouya, H. Vahabi, *Additive Manufacturing of Biopolymers* (Eds.: M. Mehrpouya, H. Vahabi), Elsevier **2023**, pp. 1–10, https://doi.org/10.1016/B978-0-323323-95151-7.00002-8.
[15] S. Sharma, V. Gupta, D. Mudgal, *Polym. Compos.* **2022**, *43*, 6749.
[16] S. Bano, A. A. Aslam, A. Khan, A. Shabbir, F. Qayyum, N. Wahab, A. Jabar, I. Ul Islam, S. L. Ng, *Process Biochem.* **2024**, *146*, 250.
[17] P. Thamarai, A. S. Vickram, A. Saravanan, V. C. Deivayanai, S. Evangeline, *Bioresour. Technol. Rep.* **2024**, *27*, 101957.
[18] A. Anjum, M. Zuber, K. M. Zia, A. Noreen, M. N. Anjum, S. Tabasum, *Int. J Biol. Macromol.* **2016**, *89*, 161.
[19] K. Eraslan, C. Aversa, M. Nofar, M. Barletta, A. Gisario, R. Salehiyan, Y. A. Goksu, *Eur. Polym. J* **2022**, *167*, 111044.
[20] B. Duan, M. Wang, W. Y. Zhou, W. L. Cheung, Z. Y. Li, W. W. Lu, *Acta Biomater.* **2010**, *6*, 4495.
[21] B. Duan, W. L. Cheung, M. Wang, *Biofabrication* **2011**, *3*, 015001.
[22] T. F. Pereira, M. A. C. Silva, M. F. Oliveira, I. A. Maia, J. V. L. Silva, M. F. Costa, R. M. S. M. Thiré, *Virt. Phys. Prototyp.* **2012**, *7*, 275.
[23] G. Colucci, M. Piano, F. Lupone, D. Baruffaldi, F. Frascella, F. Bondioli, M. Messori, *Polym. Test* **2024**, *131*, 108327.
[24] G. Colucci, F. Lupone, F. Bondioli, M. Messori, *Eur. Polym. J.* **2024**, *215*, 113197.
[25] G. Colucci, M. Piano, F. Lupone, C. Badini, F. Bondioli, M. Messori, *Mater. Today Chem.* **2023**, *33*, 101687.
[26] B. Duan, M. Wang, *J R Soc Interface* **2010**, *7*, S615.
[27] B. Duan, M. Wang, *Polym. Degrad. Stab.* **2010**, *95*, 1655.
[28] J. Schmidt, M. Sachs, C. Blümel, B. Winzer, F. Toni, K.-E. Wirth, W. Peukert, *AIP Conf. Proc.* **2015**, *1664*, 160011.
[29] N. Mys, A. Verberckmoes, L. Cardon, *Polymers* **2016**, *8*, 383
[30] N. Mys, R. Van De Sande, A. Verberckmoes, L. Cardon, *Polymers* **2016**, *8*, 150.
[31] K. T. Kunnath, S. Tripathi, S. S. Kim, L. Chen, K. Zheng, R. N. Davé, *Pharm. Res.* **2023**, *40*, 2917.
[32] J. Schmidt, W. Peukert, *Front. Chem. Eng.* **2022**, *4*, 995221.
[33] D. Li, J. Zhou, X. Ma, J. Li, *Cellulose* **2019**, *26*, 8729.
[34] A. Giubilini, G. Colucci, G. De Trane, F. Lupone, C. Badini, P. Minetola, F. Bondioli, M. Messori, *Mater. Today Sustain.* **2023**, *22*, 100379.
[35] F. M. Mwania, M. Maringa, J. G. van der Walt, *Manuf. Rev.* **2021**, *8*, 14.
[36] S. I. Martínez-Monteagudo, B. Yan, V. M. Balasubramaniam, *Food Eng. Rev.* **2017**, *9*, 143
[37] R. Levy, Z. Okun, A. Shpigelman, *Food Eng. Rev.* **2021**, *13*, 490.
[38] M. Schmid, F. Amado, G. Levy, K. Wegener, *High Value Manufacturing: Advanced Research in Virtual and Rapid Prototyping - Proceedings of the 6th International Conference on Advanced Research and Rapid Prototyping*, VR@P **2013**, pp. 95–99, https://www.scopus.com/inward/record.uri?eid=2-s2.0-84892186734&partnerID=40&md5=1eb82e94c65fa5fb6fccc5d27c130d1b.
[39] M. Schmid, A. Amado, K. Wegener, *AIP Conf. Proc.* **2015**, *1664*, 160009.
[40] A. T. Sutton, C. S. Kriewall, M. C. Leu, J. W. Newkirk, *Virt. Phys. Prototyp.* **2017**, *12*, 3.
[41] F. Lupone, E. Padovano, V. G. Lambertini, R. Sampieri, F. Casamento, S. Zecchi, C. Badini, *Adv. Eng. Mater.* **2024**, *26*, 2301345.
[42] S. Beitz, R. Uerlich, T. Bokelmann, A. Diener, T. Vietor, A. Kwade, *Materials* **2019**, *12*, 297.

[43] M. Rüther, S. H. Klippstein, S. Ponusamy, T. Rüther, H.-J. Schmid, *Powder Technol.* **2023**, *422*, 118460.
[44] D. S. Shah, K. K. Moravkar, D. K. Jha, V. Lonkar, P. D. Amin, S. S. Chalikwar, *Heliyon* **2023**, *9*, 16498.
[45] F. Lupone, E. Padovano, O. Ostrovskaya, A. Russo, C. Badini, *Compos Part A Appl. Sci. Manuf.* **2021**, *147*, 106429.
[46] R. Ajdary, N. Kretzschmar, H. Baniasadi, J. Trifol, J. V. Seppälä, J. Partanen, O. J. Rojas, *ACS Sustain. Chem. Eng.* **2021**, *9*, 2727.
[47] A. Kovalcik, *Eurobiotech J* **2021**, *5*, 48.
[48] J. Ivorra-Martinez, M. Á. Peydro, J. Gomez-Caturla, L. Sanchez-Nacher, T. Boronat, R. Balart, *Virt. Phys. Prototyp.* **2023**, *18*, 2164734.
[49] F. Selli, R. Hufenus, A. Gooneie, U. H. Erdoğan, E. Perret, *Polymers* **2022**, *14*, 200.
[50] M. Martinka Maksymiak, S. Andrä-Żmuda, W. Sikorska, H. Janeczek, P. Chaber, M. Musioł, M. Godzierz, M. Kowalczuk, G. Adamus, *Materials* **2024**, *17*, 5863.
[51] C. A. Gracia-Fernández, S. Gómez-Barreiro, J. López-Beceiro, J. Tarrío Saavedra, S. Naya, R. Artiaga, *Polym. Test* **2010**, *29*, 1002.
[52] J. Ivorra-Martinez, I. Verdu, O. Fenollar, L. Sanchez-Nacher, R. Balart, L. Quiles-Carrillo, *Polymers* **2020**, *12*, 1118.
[53] J. Ivorra-Martinez, L. Quiles-Carrillo, T. Boronat, S. Torres-Giner, J. A. Covas, *Polymers* **2020**, *12*, 1389.
[54] B. Sanders, E. Cant, C. A. Kelly, M. Jenkins, *Polymers* **2024**, *16*, 612.
[55] F. Yang, T. Jiang, G. Lalier, J. Bartolone, X. Chen, *Polym. Test* **2021**, *93*, 106920.
[56] J. Bochnia, M. Blasiak, T. Kozior, *Polymers* **2020**, *12*, 2783.